EES Solar

COMMUNICATION

View Article Online
View Journal | View Issue

Cite this: *EES Sol.*, 2025, **1**, 107

Received 5th November 2024
Accepted 3rd February 2025

DOI: 10.1039/d4el00024b

rsc.li/EESSolar

Evaporated organic–MoO_3 composite hole transport layers toward stable perovskite solar cells†

Jisu Hong, [a] Zhaojian Xu, [a] Tuo Hu,[a] Sujin Lee,[a] Manting Gui,[a] Antoine Kahn [a] and Barry P. Rand *[ab]

The release and diffusion of corrosive iodine species limits the stable operation of perovskite solar cells (PSCs). In this study, molybdenum trioxide (MoO_3) is employed for efficient oxidation of organic hole transport layers (HTLs), replacing the conventional dopant lithium bis(trifluoromethane)sulfonimide (LiTFSI) which compromises stability. Co-deposition of 2,2′,7,7′-tetra(*N*,*N*-di-*p*-tolyl)amino-9,9-spirobifluorene (spiro-TTB) and MoO_3 *via* thermal evaporation produces a HTL with appropriate ionization energy of −5.06 eV, electrical conductivity of 6.02×10^{-5} S cm^{-1}, and homogeneous morphology. To investigate the stability of PSCs using the composite HTL, three types of PSCs with different HTLs are fabricated; the 2,2′,7,7′-tetrakis[*N*,*N*-di(4-methoxyphenyl)amino]-9,9′-spirobifluorene (spiro-OMeTAD) control HTL with conventional dopants, the spiro-TTB:MoO_3 composite HTL, and the double HTL with doped spiro-OMeTAD and spiro-TTB:MoO_3 layers. The most efficient PSC with power conversion efficiency (PCE) of 21.3% is achieved by the double HTL. Since the efficient oxidation of spiro-TTB by MoO_3 and stable morphology under thermal stress mitigate iodine diffusion through the spiro-TTB:MoO_3 HTL, PSCs employing the composite HTLs demonstrate superior thermal stability, retaining 81% of their initial efficiency after 200 h aging at 85 °C.

Broader context

The instability of perovskite solar cells (PSCs) under environmental stress is a key barrier to their commercial adoption. Degradation and decomposition of halide perovskites in PSCs generate volatile byproducts such as halogen species and organic molecules. The release of iodine is particularly problematic due to its corrosive nature. Hole transport layers (HTLs) in PSCs can undergo redox reactions with oxidized iodine, facilitating iodine transport and metal corrosion. Developing a stable HTL that mitigates iodine uptake and diffusion is therefore crucial for achieving stable PSCs. Our research focuses on pre-oxidizing an organic HTL using molybdenum trioxide (MoO_3) as an oxidizing agent to prevent redox reactions with iodine. As a result, PSCs with the organic–MoO_3 composite HTL outperform control devices with conventional HTLs. The PSC with a thin layer of conventional HTL and a thicker composite HTL achieved a PCE of 21.37%, surpassing the control PSC's PCE of 20.61%. Replacing the conventional dopant, which presents stability issues with MoO_3 not only enhances the thermal stability of PSCs but also improves fabrication consistency, as evidenced by a thermal stress test at 85 °C for 200 h. The control device retained 82% of its initial PCE after only 1 h, whereas the device with the composite HTL maintained 81% of its initial performance after 200 h.

Introduction

Halide perovskites have achieved enormous breakthroughs as both single-junction solar cells and perovskite/silicon tandems, reaching power conversion efficiencies (PCEs) exceeding 26% and 33%, respectively.[1–4] However, the insufficient stability of perovskite solar cells (PSCs) remains an obstacle to commercialization. Various stressors – moisture, oxygen, illumination, elevated temperature, and electrical bias – degrade PSCs and in the process may generate volatile byproducts such as halogen species and organic molecules.[5–7] The release of iodine species and their diffusion to adjacent layers are particularly problematic due to their corrosive nature.[8–11] And also important to recognize is that for PSCs with hole transport layers (HTLs), a redox reaction between oxidized iodine species facilitates iodine transport, accelerating metal corrosion and migration.[12,13] However, the intentional oxidation (or p-doping) mitigates the redox reaction between the organic HTL material and iodine, and increases hole conductivity of the HTL.[14–16] Since HTLs play a critical role in hole carrier transport and iodine diffusion, and often determine the efficiency and stability of solar cells, developing efficient methods to oxidize HTLs is essential. Additionally, eliminating iodine transport to the metal electrodes could allow the use of less costly and noble metals; whereas Au electrodes are standard for n–i–p PSCs, practical devices would need to use metals such as Ag, Cu, or even Al.

[a]*Department of Electrical and Computer Engineering, Princeton University, Princeton, New Jersey 08544, USA. E-mail: brand@princeton.edu*

[b]*Andlinger Center for Energy and the Environment, Princeton University, Princeton, New Jersey 08544, USA*

† Electronic supplementary information (ESI) available. See DOI: https://doi.org/10.1039/d4el00024b

The benchmark HTL in n–i–p configured PSCs, 2,2′,7,7′-tetrakis(*N*,*N*-di-*p*-methoxyphenylamino)-9,9′-spirobifluorene (spiro-OMeTAD), has led to high initial PCE, but there are lingering stability concerns owing in large part to the dopant lithium bis(trifluoromethane)sulfonimide (LiTFSI). The migration of Li^+ into the perovskite layer, the hygroscopic nature of LiTFSI, and the slow oxidation procedure requiring oxygen lead to device degradation.[14,17,18] Additionally, dopant aggregation and pinhole formation in spiro-OMeTAD under thermal stress can accelerate degradation and reduce areal conductivity, while pinholes can also serve as channels for moisture and oxygen diffusion to the perovskite layers and for iodine diffusion to the metal electrodes.[14,18,19]

In this study, we utilize molybdenum trioxide (MoO_3) as an oxidizing agent *via* co-evaporation with the organic hole transport material, 2,2′,7,7′-tetra(*N*,*N*-di-*p*-tolyl)amino-9,9-spirobifluorene (spiro-TTB, Fig. 1a). MoO_3 eliminates issues related to hygroscopicity and oxygen exposure, yielding a composite HTL with a suitable ionization energy (IE) of −5.06 eV, electrical conductivity of 6.02×10^{-5} S cm^{-1}, and a smooth and homogenous morphology. Moreover, the higher intrinsic conductivity and glass transition temperature (T_g) of spiro-TTB, compared to 4,4′,4″-tris[(3-methylphenyl) phenylamino]triphenylamine (*m*-MTDATA),[15] enable more efficient and stable PSCs. Herein, three types of PSCs with different HTLs, the spiro-OMeTAD control HTL with conventional dopants, the spiro-TTB:MoO_3 composite HTL, and the double HTL comprising doped spiro-OMeTAD and spiro-TTB:MoO_3 layers, are fabricated for comparison. The PSC with the double HTL results in the highest efficiency of 21.37%, which is attributed to both perovskite layer passivation by spin coating and stable composite layer fabrication by thermal evaporation. Since the efficient oxidation of spiro-TTB by MoO_3 and stable morphology under thermal stress mitigate iodine diffusion through the composite HTL, the PSCs employing the composite HTL outlast control solar cells employing doped-spiro-OMeTAD in thermal stability tests conducted at 85 °C.

Results and discussion

The spiro-TTB : MoO_3 composite films with different spiro-TTB and MoO_3 volume ratios were fabricated by modulating the deposition rates, maintaining a total deposition rate of 1 Å s^{-1}. A pristine spiro-TTB film was also fabricated as a control. Both the pristine spiro-TTB and spiro-TTB:MoO_3 films exhibited homogeneous and smooth morphologies in atomic force microscopy (AFM) images, with root-mean-square (RMS) roughness values below 1 nm (Fig. S1, ESI†). The morphological stability of these films was assessed by annealing them at 70 °C, a temperature that solar cells can reach during outdoor operation.[20,21] Imaging before and after annealing revealed identical morphologies, with no aggregation or pinhole formation, indicating excellent morphological stability.

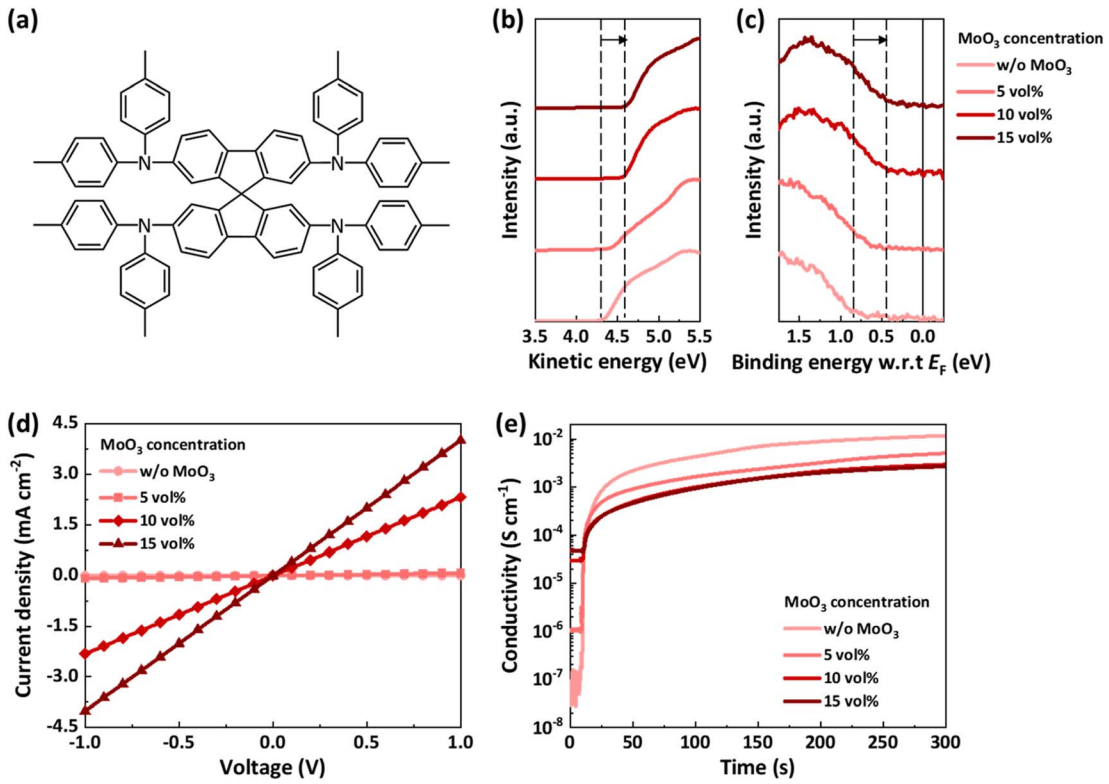

Fig. 1 (a) Molecular structure of spiro-TTB; (b and c) UPS spectra of (b) the secondary electron cut-off region and (c) the HOMO region; (d) *J*–*V* curves of the spiro-TTB:MoO_3 composite films with different MoO_3 concentrations; and (e) conductivity-time characteristics obtained from the spiro-TTB:MoO_3 composite films in an iodine-rich environment.

The effectiveness of MoO_3 as an oxidizing agent was investigated using ultraviolet photoelectron spectroscopy (UPS). The UPS spectra measured in the secondary electron cut-off region revealed a noticeable shift in the work function with the incorporation of MoO_3 (Fig. 1b). The photoemission cut-off shifted from −4.33 eV for the pristine spiro-TTB film to −4.41, −4.57, and −4.61 eV for the spiro-TTB:MoO_3 composite films with MoO_3 concentrations of 5, 10, and 15 vol%, respectively (Table 1). The UPS spectra of the highest occupied molecular orbital (HOMO) region also displayed a shift in binding energy relative to the Fermi level (E_F), from about 0.85 eV below E_F for the pristine HTL to 0.45 eV for 15 vol% loading (Fig. 1c and Table 1). The shift of E_F towards the HOMO level, attributed to the MoO_3 loading, indicates a p-doping effect of MoO_3.[22–24] The IE of the HTL remains about constant with increasing MoO_3 loading, with values of −5.18 eV for the spiro-TTB film, −5.08 eV for the composite film with 5 vol% MoO_3, and −5.06 eV for the composite films with 10 and 15 vol% MoO_3, respectively.

The p-doping effect was further evaluated through conductivity measurements. Pristine spiro-TTB films and spiro-TTB:MoO_3 composite films were fabricated, followed by the deposition of interdigitated Au electrodes. Their current density–voltage (J–V) characteristics are shown in Fig. 1d. The conductivities, calculated from the slopes of the J–V curves, were 2.09×10^{-8} S cm^{-1} for the pristine spiro-TTB film and 1.22×10^{-6}, 3.48×10^{-5}, and 6.02×10^{-5} S cm^{-1} for the composite films with 5, 10, and 15 vol% MoO_3, respectively. The results from both the UPS analysis and conductivity measurements confirm that MoO_3 effectively oxidizes spiro-TTB. Notably, the conductivity of the composite film with 15 vol% MoO_3 was comparable to the reported conductivity of LiTFSI-doped spiro-OMeTAD,[14,25] indicating that the composite film with 15 vol% MoO_3 possesses sufficient conductivity for use in PSCs.

To determine whether oxidation can prevent the redox reaction between spiro-TTB and iodine, changes in conductivity in an iodine-rich environment were monitored. Devices used for conductivity measurements were exposed to iodine vapor to observe the redox interaction between spiro-TTB and iodine, with conductivity recorded as a function of time (Fig. 1e). The initial and saturated conductivity levels observed in the devices with varying MoO_3 concentrations are noteworthy. The pristine spiro-TTB film exhibited a five-orders-of-magnitude increase in conductivity, indicating high reactivity with iodine, whereas the composite films with 10 and 15 vol% MoO_3 showed a more moderate increase of two orders of magnitude. When spiro-TTB is oxidized by MoO_3, fewer active sites exist for oxidation by iodine, resulting in a smaller increase in conductivity. These findings suggest that MoO_3 serves as an effective oxidizing agent, enhancing both the conductivity and stability of spiro-TTB in the presence of iodine.

The hole-transporting and iodine-blocking properties of the spiro-TTB:MoO_3 layer were assessed by fabricating conventional formamidinium lead iodide ($FAPbI_3$)-based PSCs. These devices featured a configuration of glass/indium tin oxide (ITO)/SnO_2/$FAPbI_3$/HTL/top electrode (Ag or Au), utilizing three distinct HTLs: the control HTL (150 nm of spiro-OMeTAD doped with conventional dopants), the double HTL (50 nm of doped spiro-OMeTAD and 100 nm of spiro-TTB:MoO_3 with 15 vol% of MoO_3), and the composite HTL (5 nm of spiro-TTB and 145 nm of spiro-TTB:MoO_3 with 15 vol% of MoO_3). The total thickness of the HTLs was maintained at 150 nm across all devices for ease of comparison. A spiro-TTB interlayer was introduced to avoid direct contact between the perovskite and MoO_3 in the PSCs with the composite HTL. Before testing the three HTLs integrated into PSCs, the spiro-TTB:MoO_3 composite layer was optimized by varying the MoO_3 concentration (10, 15, and 20 vol%) and the thickness of the spiro-TTB interlayer (2, 5, and 10 nm) as summarized in Fig. S2 and Table S1.† Statistical analysis was performed on six devices. The J–V curves for the PSCs with Ag as the top electrode are shown in Fig. 2a, with the corresponding photovoltaic parameters summarized in Table 2. A statistical distribution of these parameters obtained from six devices is provided in Table S2.† The control PSC with the spiro-OMeTAD HTL achieved a PCE of 20.6%, while the PSC with the double HTL recorded the highest PCE of 21.4%. The performance of the PSC with the double HTL was compared to that of a PSC with the m-MTDATA:MoO_3 HTL (50 nm of doped spiro-OMeTAD and 100 nm of m-MTDATA:MoO_3 as HTL) from a previous study.[15] The superior PCE is attributed to improved V_{oc} and fill factor (FF), due to better energy level alignment and conductivity in PSCs with the spiro-TTB:MoO_3 HTL. The PSC with the composite HTL delivered a PCE of 18.7%, which is among the highest reported for n–i–p structured PSCs utilizing evaporated HTLs.[26–29] Furthermore, these efficiencies achieved using Ag as the top electrode are significant, as they demonstrate competitive performance to previously reported high-performing PSCs with Ag electrodes, a more cost-effective alternative to Au.[30–33]

The J–V curves measured under different scan directions revealed that the PSC with the composite HTL exhibited more pronounced hysteresis compared to the control PSC (Fig. S3 and Table S3, ESI†). This behavior can be attributed to less effective perovskite surface passivation and reduced charge extraction

Table 1 Energy levels and electrical conductivities of the spiro-TTB:MoO_3 films

MoO_3 concentration	Photoemission cut-off (eV)	E_F-HOMO (eV)	IE (eV)	Conductivity (S cm^{-1})
w/o MoO_3	−4.33	0.85	−5.18	2.09×10^{-8}
5 vol%	−4.41	0.67	−5.08	1.22×10^{-6}
10 vol%	−4.57	0.49	−5.06	3.48×10^{-5}
15 vol%	−4.61	0.45	−5.06	6.02×10^{-5}

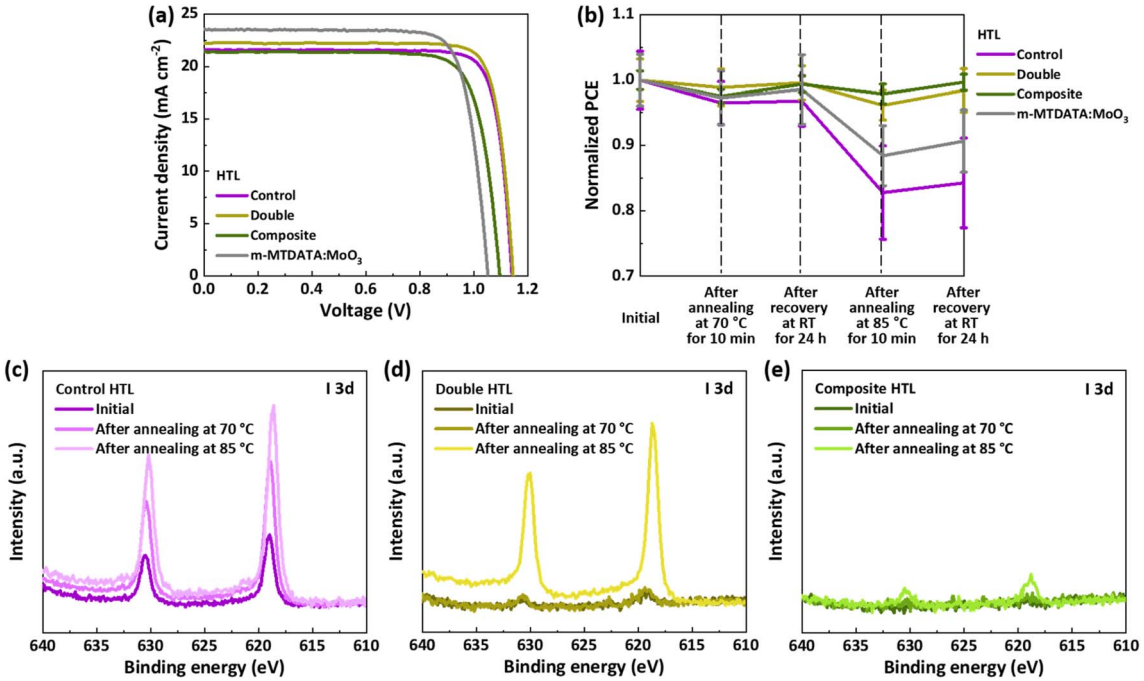

Fig. 2 (a) J–V characteristics of PSCs incorporating different HTLs. The data for the m-MTDATA:MoO_3 HTL are from an earlier study.[15] (b) Normalized PCE measured at different aging conditions, and (c–e) I 3d XPS spectra of Au electrodes peeled off from PSCs with different HTLs.

Table 2 Photovoltaic parameters of PSCs incorporating different HTLs measured in reverse scan

HTL	V_{oc} (V)	J_{sc} (mA cm^{-2})	FF (%)	PCE$_{max}$ (%)
Control	1.14	21.6	83.7	20.6
Double	1.15	22.2	83.6	21.3
Composite	1.10	21.4	79.2	18.6
m-MTDATA:MoO_3 (ref. 15)	1.05	23.6	80.5	19.9

efficiency at the perovskite/HTL interface discussed below.[34–37] To further investigate the photoresponse of the PSCs and validate the J_{sc} values obtained from the J–V curves, EQE measurements were performed as a function of wavelength (Fig. S3d, ESI†). The photoresponse of all PSCs was similar in the wavelength range of 300 to 630 nm (Beer–Lambert region), while noticeable differences in EQE were observed between 630 and 800 nm (cavity region). Since HTLs do not exhibit light absorption or emission in this region, the variations in EQE can be attributed to optical interference effects in this spectral range where the perovskite is less strongly absorbing and because MoO_3 incorporation increases refractive index. Furthermore, for all three types of devices, the integrated EQE spectra closely align with measured J_{sc} under simulated sunlight.

To understand the characteristics of the PSCs with different HTLs, the morphologies of HTLs on the perovskite were characterized by scanning electron microscopy (SEM) as shown in Fig. S4, ESI.† While all SEM images of the different HTLs reveal the presence of perovskite grains and grain boundaries, the control and double HTLs exhibit smoother morphologies, whereas the composite HTL shows a more aggregated morphology with distinct features. This suggests that the spin-coated spiro-OMeTAD layers in the control and double HTLs provide better coverage of the perovskite surface, whereas the composite layer propagated the underlying perovskite morphology. The lower V_{oc} and PCE and the large hysteresis in between the forward and reverse scans in the PSC with the composite HTL may be attributed to inefficient perovskite surface passivation as observed in the SEM images.[34,36,38]

The optical properties of the perovskite/HTL films were characterized by ultraviolet-visible (UV-vis) absorption and photoluminescence (PL) measurements, as shown in Fig. S5, ESI†. The spiro-TTB:MoO_3 composite HTL exhibited UV-vis absorption features similar to spiro-OMeTAD reported in the literature, with a primary absorption peak at 382 nm and a shoulder peak at 313 nm.[39] The broad feature around 500 nm indicates cation formation in spiro-TTB due to p-doping by MoO_3.[39,40] The UV-vis absorption spectra of the perovskite/HTL films with different HTLs revealed differences primarily in the low-wavelength region, where HTL light absorption occurs. However, these differences are more likely due to optical interference effects rather than intrinsic differences in the light absorption properties of HTLs. The PL measurements showed a characteristic emission peak at 795 nm, with variations in PL intensity among the samples. The control sample exhibited the lowest PL intensity, while the composite HTL sample showed

the highest intensity. The reduced PL quenching observed at the perovskite/composite HTL interface can be attributed to the unfavorable morphology as revealed by SEM analysis. The PSC with the double HTL was less severely affected by these factors.

The stability of PSCs with different HTLs was evaluated through a thermal stress test under varying conditions. After the initial photovoltaic characteristics were measured, the PSCs were subjected to thermal annealing at 70 °C for 10 min, followed by a recovery period at room temperature (RT) for 24 h. The PSCs were then exposed to an accelerated degradation test at 85 °C for 10 min, again followed by recovery at RT for 24 h (Fig. 2b and S6, ESI†). The control PSC exhibited only minor performance degradation at the mild temperature of 70 °C, but significant degradation was observed at 85 °C, resulting in a 17% loss of initial efficiency. Even after a 24 h recovery at RT, the performance remained diminished, with a 16% reduction in efficiency, primarily due to losses in V_{oc} and FF (Fig. S6, ESI†). In contrast, the PSCs with double and composite HTLs displayed only slight decreases in efficiency at both 70 °C and 85 °C, with full recovery upon the removal of thermal stress. Specifically, the PSC with the double HTL showed a 2% loss in initial efficiency, while the PSC with the composite HTL exhibited only a 0.3% efficiency loss, suggesting that incorporating spiro-TTB:MoO_3 layers significantly enhanced the thermal stability of PSCs. The PSC with the *m*-MTDATA:MoO_3 HTL fabricated in this study showed a 9% efficiency loss. The superior thermal stability of the spiro-TTB:MoO_3 HTL, compared to the *m*-MTDATA:MoO_3 counterpart, implies that both the elimination of problematic traditional dopants and the higher T_g of spiro-TTB contribute to the improved thermal stability.

To determine whether iodine diffusion/blocking of the HTLs was the primary factor influencing stability of the PSCs, iodine diffusion to the top electrode was monitored using X-ray photoelectron spectroscopy (XPS) for PSCs with different HTLs (Fig. 2c–e). Top Au electrodes were peeled off from the PSCs to examine the HTL/Au interface, with XPS spectra measured before and after thermal annealing. The peak intensity of the I 3d XPS spectra was normalized against the peak intensity of the Au 4f spectra. The I 3d spectra of the Au electrode with the control HTL as the underlayer showed significant peaks with high intensity under all conditions, even before annealing, indicating enhanced iodine diffusion towards the top electrode. In contrast, the I 3d spectra of the electrode with the double HTL as the underlayer displayed very low intensities before annealing and after annealing at 70 °C, suggesting that the spiro-TTB:MoO_3 layer effectively blocked iodine diffusion. However, after annealing at 85 °C, the peak intensity increased sharply. For the electrode deposited on the composite HTL, no iodine signal was detected before and after annealing at 70 °C, and only minor peaks were observed in the I 3d spectrum after annealing at 85 °C. This result supports that the reduced efficiency decrease of the PSCs with the composite HTL at 85 °C during the thermal stress test (Fig. 2b) can be attributed to the prevention of iodine diffusion to the electrode.

Given that the XPS results identified iodine diffusion as a key factor affecting the stability of PSCs with different HTLs, the stability of HTL morphology, which can significantly influence iodine diffusion, was further investigated through SEM imaging of PSCs. Cross-sectional SEM images of PSCs with different HTLs appeared identical before annealing but revealed morphological differences after annealing at 85 °C for 10 h (Fig. 3). In the control PSC, tens of nanometer-sized pinholes, which could serve as channels for significant iodine diffusion, were observed after annealing. At elevated temperatures, the volatilization of the 4-*tert*-butylpyridine (*t*BP) additive and the aggregation of LiTFSI may lead to the formation of pinholes, which in turn facilitate PSC degradation through enhanced iodine diffusion.[19,25,26] The PSC with the double HTL exhibited smaller pinholes, primarily near the interface with the perovskite layer, where the doped spiro-OMeTAD layer is present. In contrast, the composite HTL maintained an identical morphology before and after annealing, with no pinholes detected, indicating that iodine transport through the HTL was inhibited due to the less permeable nature of the composite HTL. The use of MoO_3 as an oxidizing agent, replacing conventional dopants, not only effectively oxidizes spiro-TTB but also stabilizes the HTL morphology, thereby enhancing the overall stability of the PSCs.

Since PSC degradation can be accelerated at elevated temperatures, a continuous thermal stability test was conducted at 85 °C for 200 h (Fig. 4a and S7, ESI†). The PSC with the control HTL exhibited a significant decline in PCE, with a drop to 82% of its initial value within the first hour and a further reduction to 60% after 30 h of aging. Beyond this point, the rate of degradation slowed, with the efficiency stabilizing at 56% of its initial PCE after 200 h of annealing. In contrast, the PSC with the composite HTL demonstrated greater thermal stability, showing no efficiency loss during the first 45 h of annealing and retaining 81% of its initial efficiency after 200 h. This highlights the superior thermal stability of the composite HTL compared to the control HTL. The PSC with the double HTL displayed moderate stability, maintaining 80% of its initial performance after 45 h, and 51% after 200 h, respectively. The primary contributors to PCE loss in all three cases were decreases in FF and V_{oc}.

To further assess the sensitivity of the PSCs to fabrication conditions, a thermal stability test was also conducted on PSCs fabricated in an ambient environment with relative humidity (RH) levels between 40% and 45% (Fig. S8, ESI†). All PSCs showed accelerated degradation when fabricated under these humid conditions compared to PSCs fabricated in relatively dry conditions with RH <20%. However, the rate of degradation in the control device was particularly pronounced, with a 38% loss in initial PCE within the first hour and a decline to 20% after 20 h. Unlike the PSCs fabricated under dry conditions (with RH <20%), which did not exhibit a decrease in J_{sc}, those fabricated under humid conditions showed reductions in J_{sc} along with declines in V_{oc} and FF under thermal stress, indicating susceptibility to fabrication environment. When the spiro-OMeTAD layer is spin-coated and oxidized under humid conditions, moisture can become trapped inside the spiro-OMeTAD layer due to the hygroscopic properties of LiTFSI dopant and further diffuse to the perovskite layers.[19,25] The PSCs with double and composite HTLs were more resilient,

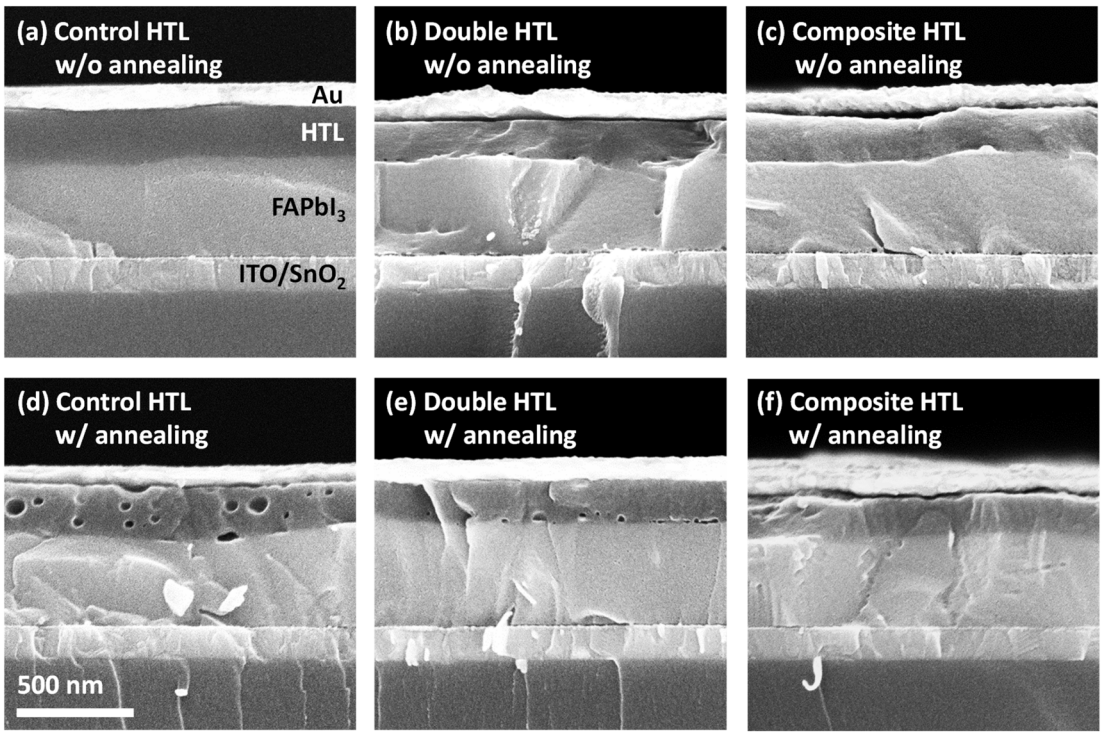

Fig. 3 Cross-sectional SEM images of PSCs with (a and d) control HTL, (b and e) double HTL, and (c and f) composite HTL. Images (a–c) show the PSCs before annealing, while (d–f) correspond to the PSCs after annealing at 85 °C for 5 h.

maintaining 80% of their initial efficiency after 20 and 55 h, respectively, and 58% and 63% of efficiency after 200 h. Notably, no decrease in J_{sc} was observed in these devices, underscoring the robustness of the spiro-TTB:MoO_3 layer. This result demonstrates the benefits of the evaporation of HTLs using MoO_3 as an oxidizing agent.

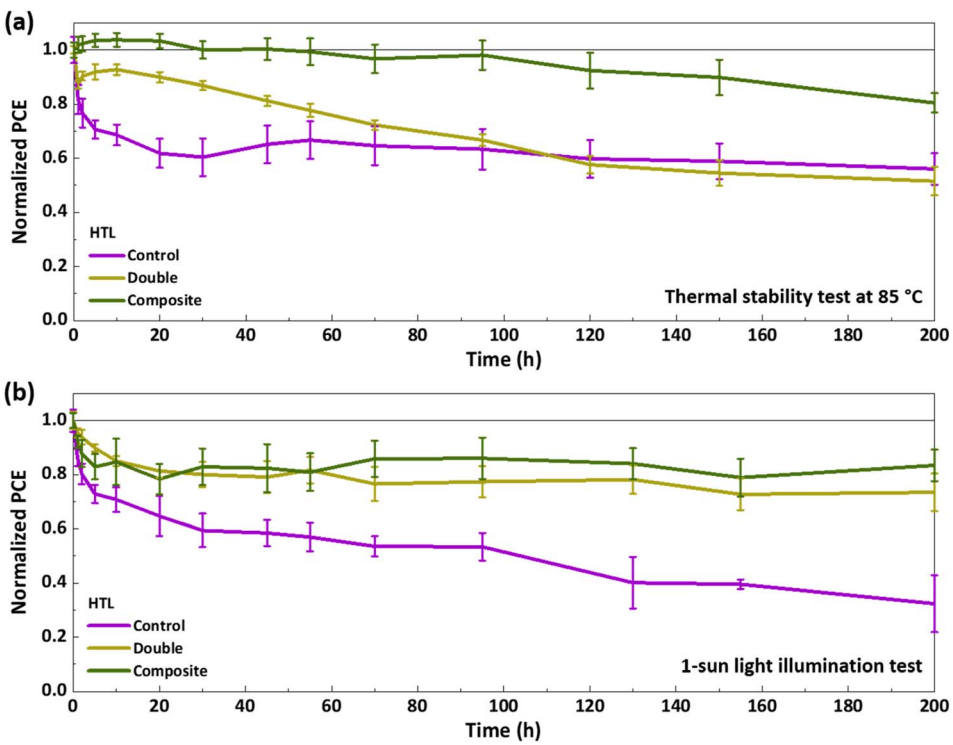

Fig. 4 Normalized PCE of the PSCs measured during (a) thermal stress testing at 85 °C and (b) continuous 1-sun light illumination.

To further assess the stability of the composite HTL under stressing conditions that promote iodide oxidation, a 1-sun light illumination test was performed. PSCs were exposed continuously to 1-sun for 200 h (Fig. 4b and S9 ESI†). The control PSC exhibited rapid degradation, with its PCE dropping to 80% of the initial value within 2 h and further declining to 32% after 200 h. In contrast, the PSC with the double HTL maintained approximately 80% of its initial PCE for the first 55 h and stabilized at 73% of the initial efficiency by the end of the test. Remarkably, the PSC with the composite HTL retained over 80% of its initial PCE throughout the 200 h illumination period. Since these results were obtained under conditions where HTL morphological stability was not a factor, the superior stability of PSCs employing the composite and double HTLs further supports the conclusion that the composite HTL effectively acts as an iodine-blocking layer.

Conclusion

A composite HTL using spiro-TTB as the organic HTL and MoO_3 as an oxidizing agent was fabricated by thermal evaporation for PSCs. Incorporating MoO_3 in place of conventional dopants for spiro-derivatives enabled efficient oxidation of spiro-TTB, resulting in an appropriate HOMO level of −5.06 eV and an electrical conductivity of 6.02×10^{-5} S cm^{-1}. The co-deposition produced a homogeneous and thermally stable morphology. Due to the efficient oxidation of spiro-TTB by MoO_3 and the thermally stable morphology, iodine diffusion through the spiro-TTB:MoO_3 composite HTL was significantly mitigated. As a result, the PSC employing the composite HTL outperformed the control device, which used conventionally doped spiro-OMeTAD by LiTFSI. The PSC with a thin doped spiro-OMeTAD layer and a thick composite layer achieved a PCE of 21.37%, surpassing the 20.61% PCE of the control PSC. In thermal stability tests conducted at 85 °C, the control device reached 82% of its initial PCE after just 1 hour of annealing, whereas the device with the composite HTL retained 81% of its initial performance after aging for 200 hours. The PSC with the double HTL exhibited moderate stability, reaching 80% of its initial efficiency for 45 hours. The 1-sun light illumination test further indicates the superior stability of the composite HTL compared to the control HTL. Additionally, PSCs with the composite HTL demonstrated robustness against humidity during the device fabrication process.

Data availability

The data supporting this article have been included as part of the ESI.†

Conflicts of interest

There are no conflicts to declare.

Acknowledgements

This work was supported by the Princeton Energy Research Fund and by the United States Department of Energy's Office of Energy Efficiency and Renewable Energy (EERE) under their Solar Energy Technology Office (SETO) award number DE-EE0010503. The authors acknowledge the use of the Imaging and Analysis Center (IAC) operated by the Princeton Materials Institute at Princeton University, which is supported in part by the Princeton Center for Complex Materials (PCCM), a National Science Foundation (NSF) Materials Research Science and Engineering Center (MRSEC; DMR-2011750).

References

1 Y. Zheng, Y. Li, R. Zhuang, X. Wu, C. Tian, A. Sun, C. Chen, Y. Guo, Y. Hua, K. Meng, K. Wu and C.-C. Chen, *Energy Environ. Sci.*, 2024, **17**, 1153–1162.
2 J. Park, J. Kim, H.-S. Yun, M. J. Paik, E. Noh, H. J. Mun, M. G. Kim, T. J. Shin and S. I. Seok, *Nature*, 2023, **616**, 724–730.
3 S. Mariotti, E. Köhnen, F. Scheler, K. Sveinbjörnsson, L. Zimmermann, M. Piot, F. Yang, B. Li, J. Warby, A. Musiienko, D. Menzel, F. Lang, S. Keßler, I. Levine, D. Mantione, A. Al-Ashouri, M. S. Härtel, K. Xu, A. Cruz, J. Kurpiers, P. Wagner, H. Köbler, J. Li, A. Magomedov, D. Mecerreyes, E. Unger, A. Abate, M. Stolterfoht, B. Stannowski, R. Schlatmann, L. Korte and S. Albrecht, *Science*, 2023, **381**, 63–69.
4 X. Y. Chin, D. Turkay, J. A. Steele, S. Tabean, S. Eswara, M. Mensi, P. Fiala, C. M. Wolff, A. Paracchino, K. Artuk, D. Jacobs, Q. Guesnay, F. Sahli, G. Andreatta, M. Boccard, Q. Jeangros and C. Ballif, *Science*, 2023, **381**, 59–63.
5 S. P. Dunfield, L. Bliss, F. Zhang, J. M. Luther, K. Zhu, M. F. A. M. van Hest, M. O. Reese and J. J. Berry, *Adv. Energy Mater.*, 2020, **10**, 1904054.
6 P. Mariani, M. Á. Molina-García, J. Barichello, M. I. Zappia, E. Magliano, L. A. Castriotta, L. Gabatel, S. B. Thorat, A. E. Del Rio Castillo, F. Drago, E. Leonardi, S. Pescetelli, L. Vesce, F. Di Giacomo, F. Matteocci, A. Agresti, N. De Giorgi, S. Bellani, A. Di Carlo and F. Bonaccorso, *Nat. Commun.*, 2024, **15**, 4552.
7 J. Zhou, Z. Liu, P. Yu, G. Tong, R. Chen, L. K. Ono, R. Chen, H. Wang, F. Ren, S. Liu, J. Wang, Z. Lan, Y. Qi and W. Chen, *Nat. Commun.*, 2023, **14**, 6120.
8 N. Li, Z. Shi, C. Fei, H. Jiao, M. Li, H. Gu, S. P. Harvey, Y. Dong, M. C. Beard and J. Huang, *Nat. Energy*, 2024, **9**, 1264–1274.
9 A. Liu, X. Li, W. Zhang, H. Yang, X. Guo, C. Lu, H. Yuan, W. Ou-Yang and J. Fang, *Adv. Funct. Mater.*, 2024, **34**, 2307310.
10 X. Li, H. Yang, A. Liu, C. Lu, H. Yuan, W. Zhang and J. Fang, *Energy Environ. Sci.*, 2023, **16**, 6071–6077.
11 Y. Kato, L. K. Ono, M. V. Lee, S. Wang, S. R. Raga and Y. Qi, *Adv. Mater. Interfaces*, 2015, **2**, 1500195.
12 Z. Xu, D. D. Astridge, R. A. Kerner, X. Zhong, J. Hu, J. Hong, J. A. Wisch, K. Zhu, J. J. Berry, A. Kahn, A. Sellinger and B. P. Rand, *J. Am. Chem. Soc.*, 2023, **145**, 11846–11858.
13 R. A. Kerner, S. Heo, K. Roh, K. MacMillan, B. W. Larson and B. P. Rand, *ACS Energy Lett.*, 2021, **6**, 501–508.

14 S. You, H. Zeng, Y. Liu, B. Han, M. Li, L. Li, X. Zheng, R. Guo, L. Luo, Z. Li, C. Zhang, R. Liu, Y. Zhao, S. Zhang, Q. Peng, T. Wang, Q. Chen, F. T. Eickemeyer, B. Carlsen, S. M. Zakeeruddin, L. Mai, Y. Rong, M. Grätzel and X. Li, *Science*, 2023, **379**, 288–294.
15 J. Hong, Z. Xu, D. Lungwitz, J. Scott, H. M. Johnson, Y.-H. Kim, A. Kahn and B. P. Rand, *ACS Energy Lett.*, 2023, **8**, 4984–4992.
16 T. H. Schloemer, J. A. Christians, J. M. Luther and A. Sellinger, *Chem. Sci.*, 2019, **10**, 1904–1935.
17 Y. Shen, K. Deng and L. Li, *Small Methods*, 2022, **6**, 2200757.
18 L. Nakka, Y. Cheng, A. G. Aberle and F. Lin, *Adv. Energy Sustainability Res.*, 2022, **3**, 2200045.
19 M. Hu, X. Wu, W. L. Tan, B. Tan, A. D. Scully, L. Ding, C. Zhou, Y. Xiong, F. Huang, A. N. Simonov, U. Bach, Y.-B. Cheng, S. Wang and J. Lu, *ACS Appl. Mater. Interfaces*, 2020, **12**, 8260–8270.
20 M. Jošt, B. Lipovšek, B. Glažar, A. Al-Ashouri, K. Brecl, G. Matič, A. Magomedov, V. Getautis, M. Topič and S. Albrecht, *Adv. Energy Mater.*, 2020, **10**, 2000454.
21 S. Pescetelli, A. Agresti, G. Viskadouros, S. Razza, K. Rogdakis, I. Kalogerakis, E. Spiliarotis, E. Leonardi, P. Mariani, L. Sorbello, M. Pierro, C. Cornaro, S. Bellani, L. Najafi, B. Martín-García, A. E. Del Rio Castillo, R. Oropesa-Nuñez, M. Prato, S. Maranghi, M. L. Parisi, A. Sinicropi, R. Basosi, F. Bonaccorso, E. Kymakis and A. Di Carlo, *Nat. Energy*, 2022, **7**, 597–607.
22 N. Sakai, R. Warren, F. Zhang, S. Nayak, J. Liu, S. V. Kesava, Y.-H. Lin, H. S. Biswal, X. Lin, C. Grovenor, T. Malinauskas, A. Basu, T. D. Anthopoulos, V. Getautis, A. Kahn, M. Riede, P. K. Nayak and H. J. Snaith, *Nat. Mater.*, 2021, **20**, 1248–1254.
23 M. Goel, M. Siegert, G. Krauss, J. Mohanraj, A. Hochgesang, D. C. Heinrich, M. Fried, J. Pflaum and M. Thelakkat, *Adv. Mater.*, 2020, **32**, 2003596.
24 B. Wegner, D. Lungwitz, A. E. Mansour, C. E. Tait, N. Tanaka, T. Zhai, S. Duhm, M. Forster, J. Behrends, Y. Shoji, A. Opitz, U. Scherf, E. J. W. List-Kratochvil, T. Fukushima and N. Koch, *Adv. Sci.*, 2020, **7**, 2001322.
25 F. M. Rombach, S. A. Haque and T. J. Macdonald, *Energy Environ. Sci.*, 2021, **14**, 5161–5190.
26 G. Du, L. Yang, C. Zhang, X. Zhang, N. Rolston, Z. Luo and J. Zhang, *Adv. Energy Mater.*, 2022, **12**, 2103966.
27 E. Aydin, J. Liu, E. Ugur, R. Azmi, G. T. Harrison, Y. Hou, B. Chen, S. Zhumagali, M. De Bastiani, M. Wang, W. Raja, T. G. Allen, A. u. Rehman, A. S. Subbiah, M. Babics, A. Babayigit, F. H. Isikgor, K. Wang, E. Van Kerschaver, L. Tsetseris, E. H. Sargent, F. Laquai and S. De Wolf, *Energy Environ. Sci.*, 2021, **14**, 4377–4390.
28 J. Feng, Y. Jiao, H. Wang, X. Zhu, Y. Sun, M. Du, Y. Cao, D. Yang and S. Liu, *Energy Environ. Sci.*, 2021, **14**, 3035–3043.
29 W. Ke, D. Zhao, C. R. Grice, A. J. Cimaroli, G. Fang and Y. Yan, *J. Mater. Chem. A*, 2015, **3**, 23888–23894.
30 W. Wang, X. Li, P. Huang, L. Yang, L. Gao, Y. Jiang, J. Hu, Y. Gao, Y. Che, J. Deng, J. Zhang and W. Tang, *Adv. Mater.*, 2024, **36**, 2407349.
31 W. Chen, S. Liu, Q. Li, Q. Cheng, B. He, Z. Hu, Y. Shen, H. Chen, G. Xu, X. Ou, H. Yang, J. Xi, Y. Li and Y. Li, *Adv. Mater.*, 2022, **34**, 2110482.
32 H. B. Lee, N. Kumar, M. M. Ovhal, Y. J. Kim, Y. M. Song and J.-W. Kang, *Adv. Funct. Mater.*, 2020, **30**, 2001559.
33 C. Ding, L. Yin, L. Zhang, R. Huang, S. Fan, Q. Luo, J. Lin, F. Li, C. Zhao, R. Österbacka and C.-Q. Ma, *Adv. Funct. Mater.*, 2021, **31**, 2103820.
34 Z. Zhang, L. Qiao, K. Meng, R. Long, G. Chen and P. Gao, *Chem. Soc. Rev.*, 2023, **52**, 163–195.
35 W. Xu, L. J. F. Hart, B. Moss, P. Caprioglio, T. J. Macdonald, F. Furlan, J. Panidi, R. D. J. Oliver, R. A. Pacalaj, M. Heeney, N. Gasparini, H. J. Snaith, P. R. F. Barnes and J. R. Durrant, *Adv. Energy Mater.*, 2023, **13**, 2301102.
36 L. Zhu, X. Zhang, M. Li, X. Shang, K. Lei, B. Zhang, C. Chen, S. Zheng, H. Song and J. Chen, *Adv. Energy Mater.*, 2021, **11**, 2100529.
37 W. Xiang, S. Liu and W. Tress, *Angew. Chem.*, 2021, **133**, 26644–26657.
38 S. Zhang, F. Ren, Z. Sun, X. Liu, Z. Tan, W. Liu, R. Chen, Z. Liu and W. Chen, *Small Methods*, 2024, **8**, 2301223.
39 G. Szabó and P. V. Kamat, *ACS Energy Lett.*, 2025, **10**, 330–336.
40 B. Tan, S. R. Raga, A. S. R. Chesman, S. O. Fürer, F. Zheng, D. P. McMeekin, L. Jiang, W. Mao, X. Lin, X. Wen, J. Lu, Y.-B. Cheng and U. Bach, *Adv. Energy Mater.*, 2019, **9**, 1901519.